Supplement to: Improved representation of laminar and turbulent sheet flow in subglacial drainage models

Tim Hill[1], Gwenn E. Flowers[1], Matthew J. Hoffman[2], Derek Bingham[3], Mauro A. Werder[4,5]

[1]*Department of Earth Sciences, Simon Fraser University, Burnaby, BC, Canada*

[2]*Fluid Dynamics and Solid Mechanics Group, Los Alamos National Laboratory, Los Alamos, NM, USA*

[3]*Department of Statistics and Actuarial Science, Simon Fraser University, Burnaby, BC, Canada*

[4]*Laboratory of Hydraulics, Hydrology and Glaciology (VAW), ETH Zurich, Zurich, Switzerland*

[5]*Swiss Federal Institute for Forest, Snow and Landscape Research (WSL), Birmensdorf, Switzerland*

Correspondence: Tim Hill <tim_hill_2@sfu.ca>

S1 METHODS

S1.1 Model parameters

To apply GlaDS to a synthetic Greenlandic catchment with seasonally varying melt forcing, key model parameters (bed bump height h_r and wavelength l_r, the width of sheet flow contributing to channel discharge l_c, and channel conductivity k_c) are increased in magnitude to accommodate the larger scale of the Greenland catchment compared to an alpine glacier catchment and the transient, surface input-dominated drainage characteristic of Greenland rather than steady Antarctic hydrology (Table 1). We envision the controlling bed bump scale for subglacial drainage beneath the Greenland Ice Sheet to be larger (bed bump length $l_\mathrm{r} = 10\,\mathrm{m}$ and height $h_\mathrm{r} = 0.5\,\mathrm{m}$) than is often used for alpine glacier hydrology (e.g., $l_\mathrm{r} = 2\,\mathrm{m}$, $h_\mathrm{r} = 0.1\,\mathrm{m}$ for Gornergletscher; Werder and others, 2013) or steady state Antarctic hydrology (e.g., $l_\mathrm{r} = 2$–$4\,\mathrm{m}$, $h_\mathrm{r} = 0.08$–$0.1\,\mathrm{m}$; Dow and others, 2022; Hager and others, 2022). This bedrock bump scale is smaller than that used by Cook and others (2022) for transient simulations of Store Glacier ($l_\mathrm{r} = 100\,\mathrm{m}$, $h_\mathrm{r} = 1\,\mathrm{m}$) and larger than that of Downs and others (2018) for a synthetic Greenland catchment ($l_\mathrm{r} = 2\,\mathrm{m}$, $h_\mathrm{r} = 0.1\,\mathrm{m}$). The channel conductivity $k_\mathrm{c} = 0.5\,\mathrm{m}^{3/2}\,\mathrm{kg}^{-1/2}$ is slightly larger than that of Cook and others (2022) and Downs and others (2018) ($k_\mathrm{c} = 0.1\,\mathrm{m}^{3/2}\,\mathrm{kg}^{-1/2}$), larger than the typical range for steady Antarctic hydrology ($k_\mathrm{c} = 0.05\,\mathrm{m}^{3/2}\,\mathrm{kg}^{-1/2}$; Dow and others, 2022) and at the upper end of the range considered by Hager and others (2022) (0.005–$0.5\,\mathrm{m}^{3/2}\,\mathrm{kg}^{-1/2}$). The remainder of the model parameter values in Table 1

are within the range found in the literature for GlaDS and similar models (e.g., Werder and others, 2013; Downs and others, 2018; Cook and others, 2022; Dow and others, 2022; Hager and others, 2022).

S1.2 Cavity opening mechanisms

By default, GlaDS allows cavities to creep open when water pressure exceeds ice overburden. Fundamentally, we expect that unrepresented physics would evolve the drainage system towards a state with $p_\mathrm{w} \leq p_\mathrm{i}$ (e.g., Tsai and Rice, 2010; Dow and others, 2015). We have also found that allowing creep opening in the model setup presented here results in unrealistic channel configurations and water pressure. When the drainage system becomes overpressurized and creep opening is allowed, cavities expand to heights much larger than the bed bump height, inhibiting channelization within overpressurized regions. With channels only developing in regions with pressure below overburden, the model struggles to evacuate meltwater from the enlarged cavities, resulting in water pressure above overburden for the entire melt season. Therefore, for conceptual and practical reasons, we have set the creep constant $\tilde{A} = 0$ where $p_\mathrm{w} > p_\mathrm{i}$, capping the cavity height at the bed bump height. This cap is a practical way to maintain channels within overpressurized regions and appears to be a better modelling choice than the default behaviour to overcome unrepresented physical mechanisms. While the creep constant when $p_\mathrm{w} > p_\mathrm{i}$ is not often reported in tables of GlaDS model parameters (e.g., Werder and others, 2013; Cook and others, 2020; Dow and others, 2022; Ehrenfeucht and others, 2023), other models cap effective pressure $N \geq 0$ to avoid cavities and channels opening by ice creep (e.g., Hoffman and others, 2018; Sommers and others, 2018).

S1.3 Distributed flux models

S1.3.1 Darcy-Weisbach turbulent flow exponents

For a fluid with density ρ, the Darcy-Weisbach equation computes the fluid potential gradient required for the fluid to flow with velocity v according to (e.g., Moody, 1944; Brown, 2002),

$$|\nabla\phi| = f_\mathrm{D}\frac{\rho}{2}\frac{v^2}{D_\mathrm{H}} \tag{S.1}$$

for Darcy friction factor f_D and hydraulic radius D_H. For flow through an arbitrarily shaped conduit, the hydraulic radius is $D_\mathrm{H} = 4A/P$, where A is the cross-sectional area and P is the perimeter.

The Darcy-Weisbach equation is an empirical equation, yet with roots in Bernoulli's principle, developed

for computing the design requirements of pipe flow (e.g., Brown, 2002). From a practical perspective, the friction factor f_{D} would be computed from known material properties (i.e., material roughness) and the intended Reynolds number of the flow (i.e., from the Moody diagram; Moody, 1944), in order to compute the required pipe radius, for example. The Darcy-Weisbach equation is useful for subglacial drainage modelling since it is simple compared to solving the fluid momentum balance that is applicable in both laminar and turbulent regimes and for flow through "full" drainage elements.

It is instructive to rewrite Eq. (S.1) for the case of flow through a pipe with a circular cross section to see how the "flow exponents" α and β in the subglacial discharge parameterization arise (Eq. 12 of Werder and others, 2013). In this case, the hydraulic radius reduces to $D_{\mathrm{H}} = D$ for pipe diameter D. For a discharge Q and area S, the velocity must be $v = Q/S$. All together, and taking $D = 2\sqrt{\frac{S}{\pi}}$ (compare to Eq. 13 of Werder and others, 2013), Eq. (S.1) can be written in the form of the GlaDS flux parameterization

$$Q = \frac{2}{\sqrt{\rho f_{\mathrm{D}}}\pi^{1/4}} S^{5/4} |\nabla\phi|^{1/2}. \tag{S.2}$$

From pipe-flow experiments and from the Moody diagram (Fig. 1), fully turbulent flow corresponds to a constant f_{D}. This means that, in the fully turbulent limit, this form derived from the Darcy-Weisbach equation is identical to the GlaDS flux parameterization with $\alpha = 5/4$ and $\beta = 3/2$ (Werder and others, 2013).

Similar steps lead to the conclusion that $\alpha = 3/2$ for the distributed flow parameterization. In the spirit of the bulk-averaged approach to the drainage through a "subglacial water sheet" (e.g., Werder and others, 2013), consider flow at velocity v through a gap with average height h. Before we proceed with Eq. (S.1), we need an expression for the hydraulic radius. For parallel lower and upper boundaries (i.e., the gap height is exactly h everywhere), the hydraulic for flow through a gap of width w is

$$D_{\mathrm{H}} = 4\frac{wh}{2(w+h)} \approx 2h, \tag{S.3}$$

where the approximation assumes that $w \gg h$. This approximation should hold in the subglacial context, where the width of the flow is on the scale of kilometers and the vertical extent is on the scale of meters. While we don't envision the gap height being uniformly h everywhere for physical drainage elements comprising the "distributed drainage system", the shallow aspect ratio of the subglacial drainage system should ensure the applicability of this hydraulic radius. By writing the discharge-per-unit-width as

$q = vh$, we can write Eq. (S.1) in the context of sheet-like flow as

$$q = 2\frac{1}{\sqrt{\rho f_{\mathrm{D}}}} h^{3/2} |\nabla\phi|^{1/2}. \tag{S.4}$$

Once again, taking the fully turbulent limit and assuming f_{D} is constant (Fig. 1), this expression is in the form of the GlaDS sheet-flow model with $\alpha = 3/2$ (rather than 5/4, as is usually suggested for fully turbulent flow; Werder and others, 2013) and $\beta = 3/2$.

S1.3.2 Implementation of the transition flux parameterization

The Transition flux parameterization as presented in the main text is

$$-k_{\mathrm{s}} h^3 \nabla\phi = \mathbf{q} + \omega \mathrm{Re} \left(\frac{h}{h_b}\right)^{3-2\alpha_{\mathrm{s}}} \mathbf{q}, \tag{S.5}$$

for conductivity k_{s}, hydraulic potential ϕ, discharge-per-unit-width q, Reynolds number Re, sheet thickness h, bed bump height h_{b}, and turbulent flow exponent α_{s}. Here we present the brief steps required to explicitly solve the parameterization for the flux q. Substituting the Reynolds number ($\mathrm{Re} = \frac{\mathrm{q}}{\nu}$) yields a quadratic equation in terms of $q = |\mathbf{q}|$,

$$-k_{\mathrm{s}} h^3 \nabla\phi = \mathbf{q} + \frac{\omega}{\nu} \left(\frac{h}{h_b}\right)^{3-2\alpha_{\mathrm{s}}} q\mathbf{q}. \tag{S.6}$$

This equation can be solved exactly for $\mathbf{q}$,

$$\mathbf{q} = -\frac{\nu}{2\omega} \left(\frac{h_0}{h}\right)^{3-2\alpha_{\mathrm{s}}} \left(-1 + \sqrt{1 + 4\frac{\omega}{\nu} \left(\frac{h}{h_0}\right)^{3-2\alpha_{\mathrm{s}}} k h^3 |\nabla\phi|}\right) \frac{\nabla\phi}{|\nabla\phi|}. \tag{S.7}$$

This expression simplifies for the $\alpha_{\mathrm{s}} = 3/2$ case (i.e., for the Turbulent 3/2 model),

$$\mathbf{q} = -\frac{\nu}{2\omega} \left(-1 + \sqrt{1 + 4\frac{\omega}{\nu} k h^3 |\nabla\phi|}\right) \frac{\nabla\phi}{|\nabla\phi|}. \tag{S.8}$$

This simplified expression and Eq. (S.7) are no more difficult to evaluate numerically than the standard GlaDS parameterization, as they both require evaluating a single spatial derivative ($\nabla\phi$), and are written explicitly so no iteration is required.

S1.3.3 Turbulent conductivity scaling

Since the conductivity for the turbulent model is specified in different units (that depend on the turbulent flow exponent α_s) than the laminar and transition models, the turbulent conductivity needs to be scaled appropriately to ensure a valid comparison between flux models.

The critical water layer thickness that results in a Reynolds number equal to the transition threshold is computed from the laminar model by setting $\omega\mathrm{Re} = \omega\mathrm{q}/\nu = 1$,

$$h_\mathrm{crit}^3 = \frac{\nu}{\omega}\frac{1}{k_\mathrm{s}|\nabla\phi|}. \tag{S.9}$$

We solve for the turbulent conductivity by setting the laminar and turbulent models equal with $h = h_\mathrm{crit}$,

$$k_\mathrm{t} h_\mathrm{crit}^{\alpha_\mathrm{s}}|\nabla\phi|^{1/2} = k_\mathrm{s} h_\mathrm{crit}^3|\nabla\phi|. \tag{S.10}$$

Therefore, the turbulent conductivity is given by

$$k_\mathrm{t} = k_\mathrm{s} h_\mathrm{crit}^{3-\alpha_\mathrm{s}}|\nabla\phi|^{1/2}. \tag{S.11}$$

When $\alpha_\mathrm{s} = 3/2$, the $\nabla\phi$-dependence drops out of the expression for k_t. When $\alpha_\mathrm{s} = 5/4$, the potential gradient is set to the average value assuming water pressue is equal to overburden for a given geometry.

S1.4 Surface melt forcing

To derive realistic yet idealized surface melt forcing, we use temperatures recorded at the PROMICE KAN_L weather station (How and others, 2022) to drive a degree-day melt model. Before using the temperature record to drive the melt model, we find a melt year that is representative according to the total volume and duration of surface melt.

For the record of diurnal mean temperatures spanning 2009–2022, we compute the cumulative positive degree-days as a proxy for total melt volume and the melt season duration. Cumulative positive degree-days are computed directly from the diurnal mean temperatures. The beginning of the melt season is defined as the first day with positive diurnal mean temperatures on the n following consecutive days. The end of the melt season is defined analogously as the last day with positive diurnal mean temperatures on the n preceding consecutive days. We compute the melt season duration for $n = 2, 3, 5$ days to derive

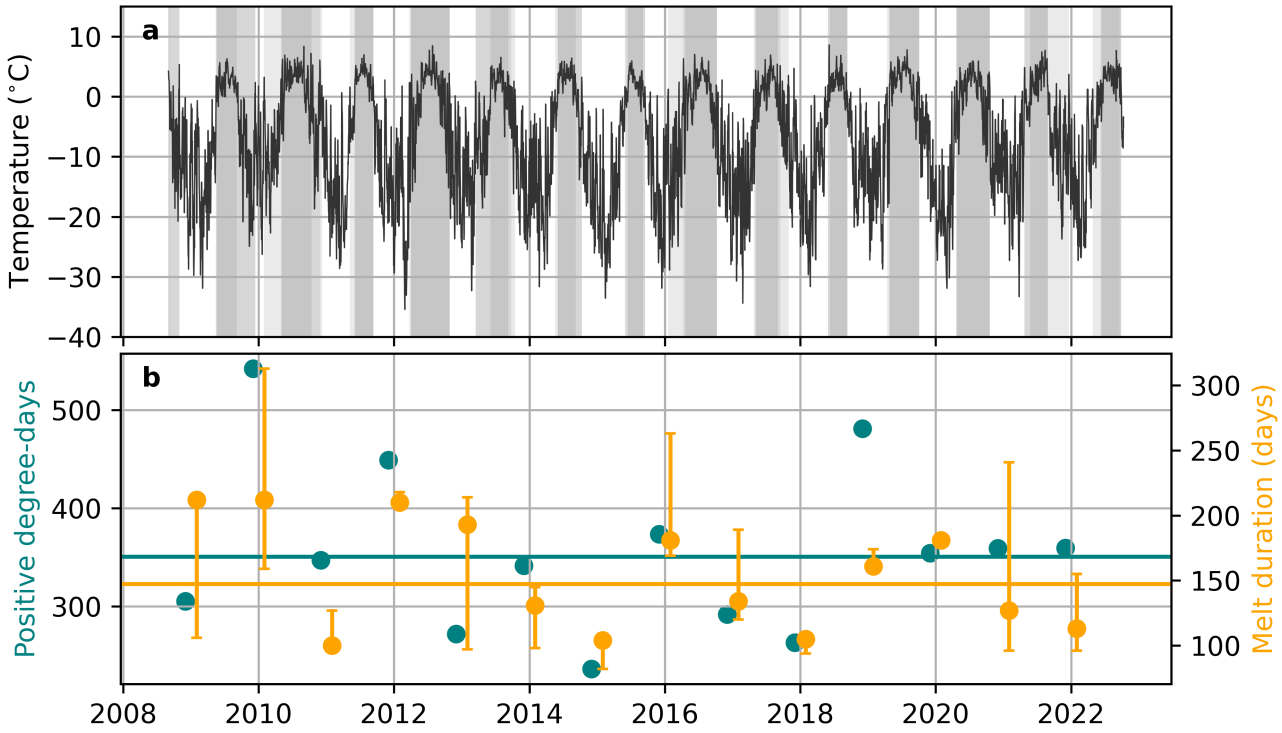

Fig. S1. KAN_L automated weather station (AWS) temperature record (How and others, 2022), positive degree-days and melt season durations. (a) Diurnal mean AWS temperature. Shaded grey regions indicate the melt season, defined as consecutive positive-degree days for 2, 3, or 5 days to derive a range of melt season durations. (b) Cumulative positive degree-days (left axis) and melt season duration (right axis). Horizontal lines indicate the median positive degree-days and melt season duration. Error bars for the melt season duration show the minimum and maximum melt season duration from the ensemble of melt season definitions. The 3-day definition is used to plot the representative melt season duration. Based on the total positive degree-days and melt season duration near the 2009–2022 medians, we select 2014 as the representative melt year.

lower and upper bounds on the melt season duration. The difference between the bounds is used as an approximate indicator of short-duration melt events outside the core melt season with nearly continuous positive temperatures.

The 14-year record of diurnal mean temperature record, positive degree-days and melt season duration are compared in Fig. S1. Based on the median positive degree-days and melt season duration, we choose 2014 as a representative melt year.

S1.5 Moulin design

Surface runoff is integrated within supraglacial catchments and routed through moulins to localize melt inputs to the bed. For the synthetic domain geometry, catchment and moulin designs are generated from a space-filling Latin hypercube design that is scaled to approximate the observed relative density of moulins

within elevation bands.

The observed density of moulins as a function of elevation is derived from satellite-based supraglacial hydrology mapping of a portion of the southwest Greenland ice sheet (Yang and Smith, 2016) (Fig. S2). Moulin designs are generated by drawing a sample of y (across-glacier) and z (elevation) coordinates, which are then scaled to fill the complete domain-width and elevation range, with the elevation samples conforming to the observed distribution. The inverted surface elevation function is used to transform the elevations to x positions. The (x, y) coordinates are then used as the centers of supraglacial catchments and moulins are placed at the lowest node within each catchment subject to:

1. $x \geq 5\,\mathrm{km}$ to mimic the effects of high surface slopes and crevasses (Werder and others, 2013),
2. the minimum distance between moulins is 2.5 km, and
3. moulins aren't placed on boundary nodes.

Surface melt is integrated within each catchment and instantaneously routed through the catchment into the outlet moulin.

Fig. S2 illustrates the process to obtain a moulin design. The deviation between the synthetic and Yang and Smith (2016) density between 500 and 600 m elevation is due to the first condition above. This condition results in four moulins placed at $x = 5\,\mathrm{km}$, and since the area within the 500 to 600 m elevation bin is small relative to the area within higher bins due to the high surface slope near the terminus, the observed density is artificially high between 500 and 600 m. The remainder of the deviations are a result of the random nature of the moulin placement scheme.

S1.6 Mesh sensitivity

To assess the sensitivity of modelled subglacial drainage to the numerical mesh, we ran steady state simulations with 10 meshes with the number of nodes varying between 107 and 16169 (Fig. S3). Each mesh refinement case is run with identical geometry and parameters. The total prescribed moulin discharge is identical, but the position of moulins changes since moulins must be placed on mesh nodes. To reposition moulins for each mesh, moulin positions are interpolated from the reference case (4156 nodes) to the nearest node in the mesh under consideration, and the moulin discharge is directly transferred to the newly repositioned moulin. For the coarse meshes, this approach means that sometimes multiple moulins

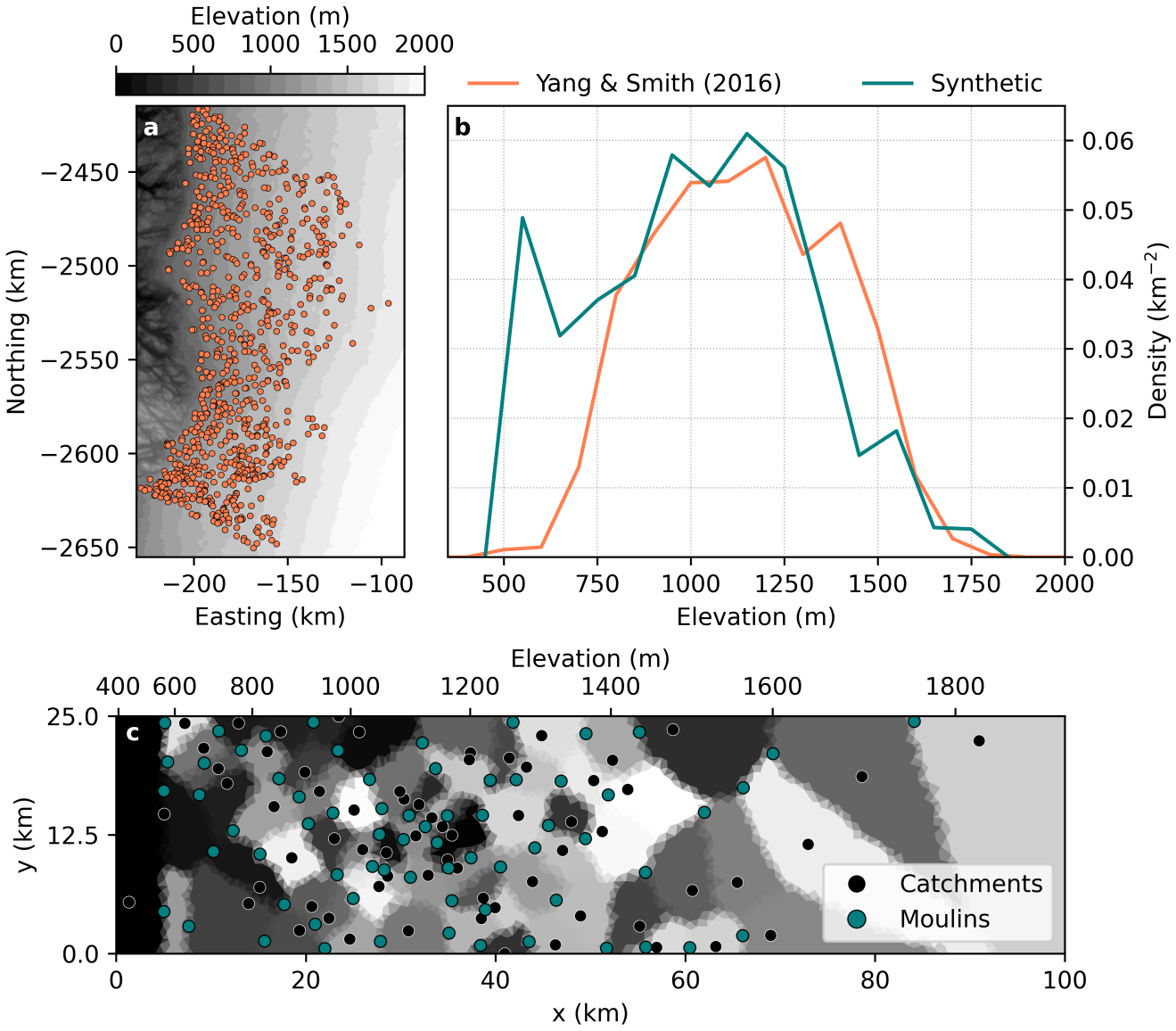

Fig. S2. Summary of the scheme used to generate the synthetic moulin design. (a) ArcticDEM 500 m mosaic surface elevation (Porter and others, 2018) and moulin positions mapped from a 19 August 2013 panchromatic Landsat 8 image by Yang and Smith (2016). (b) Moulin density in 100 m elevation bins derived from the Yang and Smith (2016) dataset and for the synthetic moulin design. (c) Synthetic catchment centers, moulin positions, and catchment areas (coloured polygons), with distance (bottom) and surface elevation (top) scales.

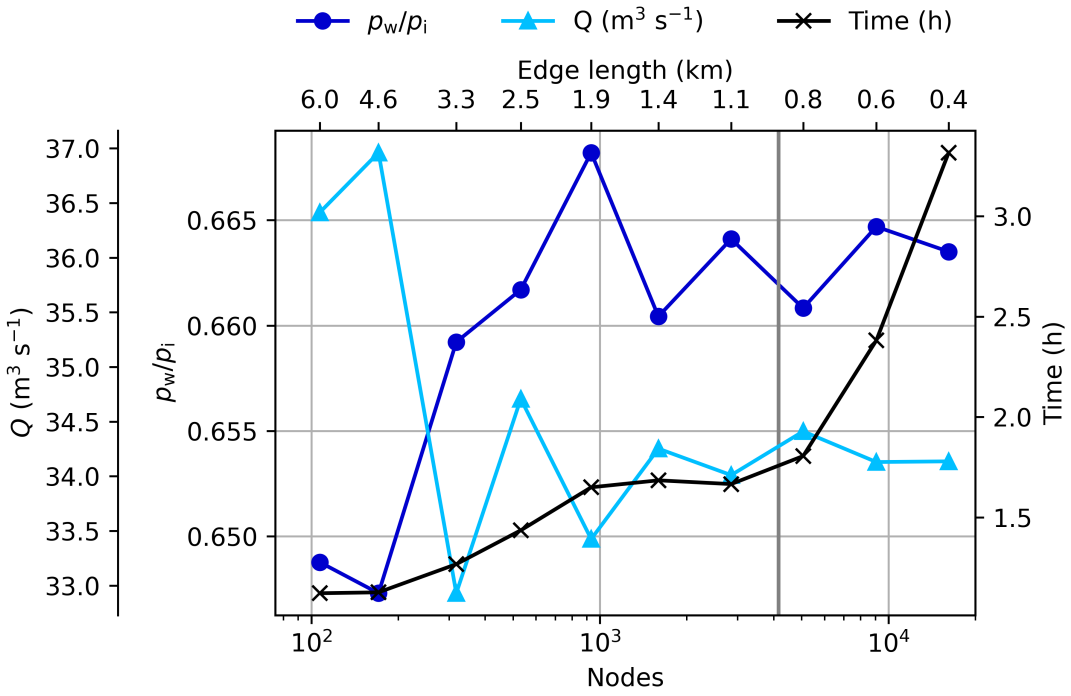

Fig. S3. Results of the mesh refinement test. Mean floatation fraction (inner left axis), total channel discharge (outer left axis) at $x = 30 \pm 2.5$ km and total model runtime (right axis) for 10 meshes with increasing number of nodes. The default mesh in the main text contains 4156 nodes (indicated by the vertical grey line).

from the reference mesh are placed at the same node. When this happens, the moulin discharge is the sum of the discharge for original moulins that are now co-located.

The floatation fraction and channel discharge converge as the number of nodes increases as well as expected for GlaDS (Fig. S3), where the random orientation of edges has some influence on channel positions (e.g., Werder and others, 2013, Fig. A1). Some of the residual variance in the mesh refinement curves may also be a result of interpolating moulins to new node positions. Nevertheless, the reference mesh (4156 nodes) represents an appropriate balance between convergence and model runtime.

S2 RESULTS

S2.1 Steady state comparison

Fig. S4 shows the floatation fraction, Reynolds number, and channel discharge at the end of the 100 year spin-up, when the drainage system has reached a steady state.

S2.2 Tabulated floatation fraction and computation time

Table S1 compares winter and summer pressures for all models within 5 km-wide bands centred at $x = 15$, 30, and 70 km. Table S2 compares the total computation time for the main series of simulations. These times represent the total time for spinup and transient simulations.

S2.3 KAN scenario Reynolds number

To assess the consistency of the laminar and turbulent assumptions for the KAN forcing scenario, Fig. S5 presents the seasonal evolution of the Reynolds number. All models result in turbulent flow in the early melt season, with the highest Reynolds number produced by the laminar model in the early melt season.

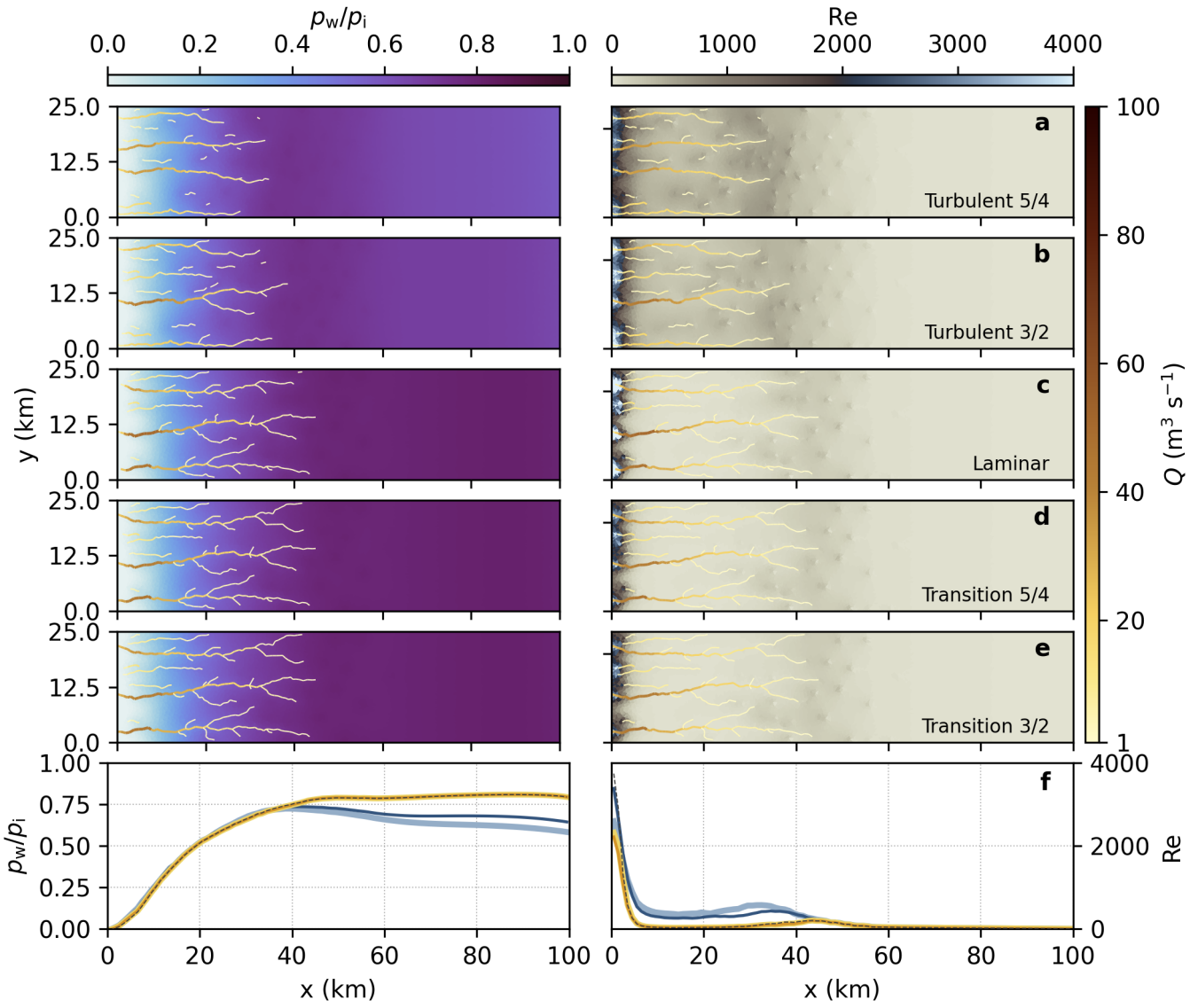

Fig. S4. Floatation fraction and Reynolds number for steady state simulation. (a–e) Floatation fraction (left) and Reynolds number ($\mathrm{Re} = \frac{q}{\nu}$; right) for the five sheet-flux parameterizations. (f) Width-averaged profiles of floatation fraction (left) and Reynolds number (right).

Table S1. Water pressure normalized by overburden (floatation fraction) for synthetic and KAN surface melt forcing scenarios. Winter floatation fraction is computed as the width-averaged value at the specified position (±2.5 km) during the two months preceding the initial onset of surface melt. The reported summer floatation fraction values are the 95th-percentile width-averaged water pressure produced during the melt season within ±2.5 km of the specified position. The bracketed number beside summer floatation fractions for the KAN scenario indicates the number of days water pressure exceeded overburden. Water pressure does not exceed overburden in the Synthetic scenario. "Turb" refers to turbulent models, "Trans" refers to Transition models, and the fraction (5/4 or 3/2) identifies the turbulent flow exponent α_s value.

			Floatation fraction				
Scenario	Season	Distance from terminus	Turb 5/4	Turb 3/2	Laminar	Trans 5/4	Trans 3/2
Synthetic	Winter	15 km	0.138	0.231	0.466	0.466	0.468
		30 km	0.430	0.511	0.670	0.671	0.672
		70 km	0.616	0.675	0.798	0.798	0.798
	Summer	15 km	0.751	0.742	0.698	0.728	0.757
		30 km	0.829	0.826	0.811	0.828	0.847
		70 km	0.669	0.696	0.799	0.799	0.800
KAN	Winter	15 km	0.144	0.234	0.466	0.467	0.468
		30 km	0.436	0.513	0.670	0.671	0.672
		70 km	0.620	0.676	0.798	0.798	0.798
	Summer	15 km	0.98 (8)	1.03 (9)	0.960 (6)	1.03 (10)	1.07 (10)
		30 km	1.04 (9)	1.02 (10)	0.997 (6)	1.01 (9)	1.01 (11)
		70 km	0.771 (0) (0)	0.785 (0)	0.849 (0)	0.851 (0)	0.857 (0)

Table S2. Total simulation runtime in hours for synthetic and KAN scenarios (spinup and transient) and for each flux parameterization. Simulations were carried out in serial on Intel E5-2683 CPUs with 4G of memory on the Compute Canada Cedar cluster.

Model	Synthetic scenario	KAN scenario
Turbulent 5/4	0.78	8.37
Turbulent 3/2	0.64	10.39
Laminar	0.57	8.52
Transition 5/4	0.63	9.51
Transition 3/2	0.69	12.60

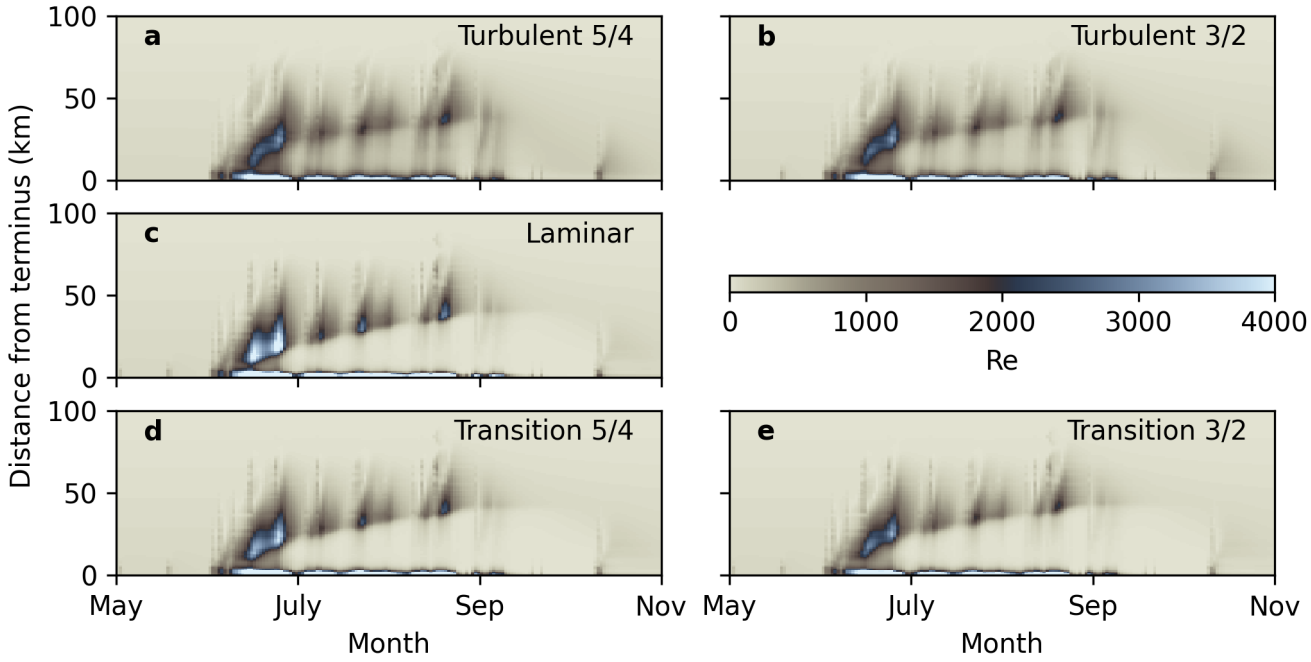

Fig. S5. Seasonal evolution of width-averaged Reynolds number with KAN forcing for Turbulent 5/4 (a), Turbulent 3/2 (b), Laminar (c), Transition 5/4 (d), and Transition 3/2 (e) models.

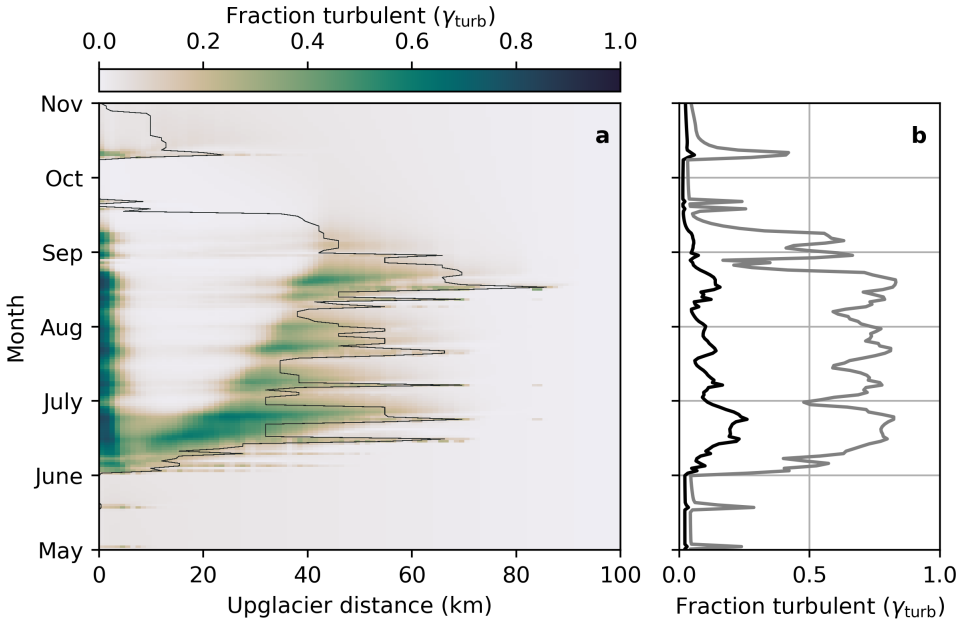

Fig. S6. Seasonal transitions between laminar and turbulent flow for the Transition 3/2 model with KAN forcing. (a) Width-averaged fraction of turbulent flow (γ_{turb}; Eq. S.13). The thin superimposed black line delineates the maximum upglacier extent of channels with discharge $Q > 1\,\text{m}^3\,\text{s}^{-1}$. (b) Domain-averaged (black) and maximum width-averaged (grey) fraction turbulent.

S2.4 Seasonal laminar turbulent partitioning

The partitioning between laminar and turbulent flow in the transition model can be quantified by comparing the size of the terms on the right-hand-side of Eq. (S.5). The contribution of laminar and turbulent flows are therefore

$$\gamma_{\text{laminar}} = \frac{q}{kh^3|\nabla\phi|} \tag{S.12}$$

$$\gamma_{\text{turb}} = \frac{\frac{\omega}{\nu}\left(\frac{h}{h_b}\right)^{3-2\alpha_s} q^2}{kh^3|\nabla\phi|}. \tag{S.13}$$

Figure S6 shows the turbulent fraction, γ_{turb}, for the KAN forcing scenario. Flow is laminar outside the melt season and above the maximum melt extent. The model also predicts laminar sheet-flow within the region of the well-developed channel network during the melt season (i.e., between ∼5 and ∼30 km from July to September). Flow partially transitions to turbulent within the upper reaches of the channel network, immediately downstream of the $Q > 1\,\text{m}^3\,\text{s}^{-1}$ contour. Flow is turbulent within the lowest ∼5 km during the melt season, however this is attributed to boundary effects.

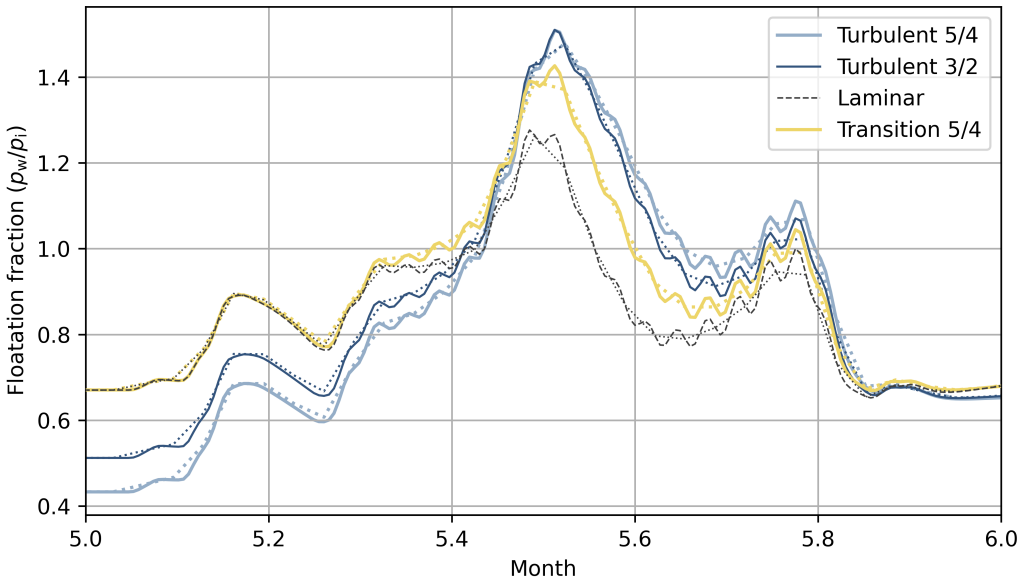

Fig. S7. Average floatation fraction within $x = 30 \pm 2.5\,\mathrm{km}$ with (solid) and without (dotted) diurnal variations in surface melt forcing for the first month of the KAN scenario melt season.

S2.5 Diurnal melt-rate variations

To assess the impact of diurnal melt-rate variations on modelled water pressure, diurnals are added to the prescribed surface melt rate. The diurnal surface melt rate, $\dot{m}_\mathrm{d}$, is computed from the seasonal KAN scenario melt rate $\dot{m}$ (Eq. 6) following

$$\dot{m}_\mathrm{d}(z,t;\Gamma) = \dot{m}(z,t;\Gamma)\left(1 - 0.5\cos\left(\frac{2\pi t}{T_\mathrm{day}}\right)\right), \tag{S.14}$$

for t the time in seconds and T_day the number of seconds per day.

Fig. S7 compares modelled floatation fraction within $x = 30 \pm 2.5\,\mathrm{km}$ with and without diurnal variations in surface melt forcing for four of the five flux parameterizations. There is little difference in floatation with and without diurnal variations, and so the relative performance of each model is not sensitive to diurnal forcing.

S2.6 Model verification

To verify the implementation of the transition models, and more broadly to compare two of the presently available implementations of GlaDS, we compare the Matlab implementation (i.e., the code from Werder and others, 2013) with the relatively newer implementation within the Ice-sheet and Sea-level System Model

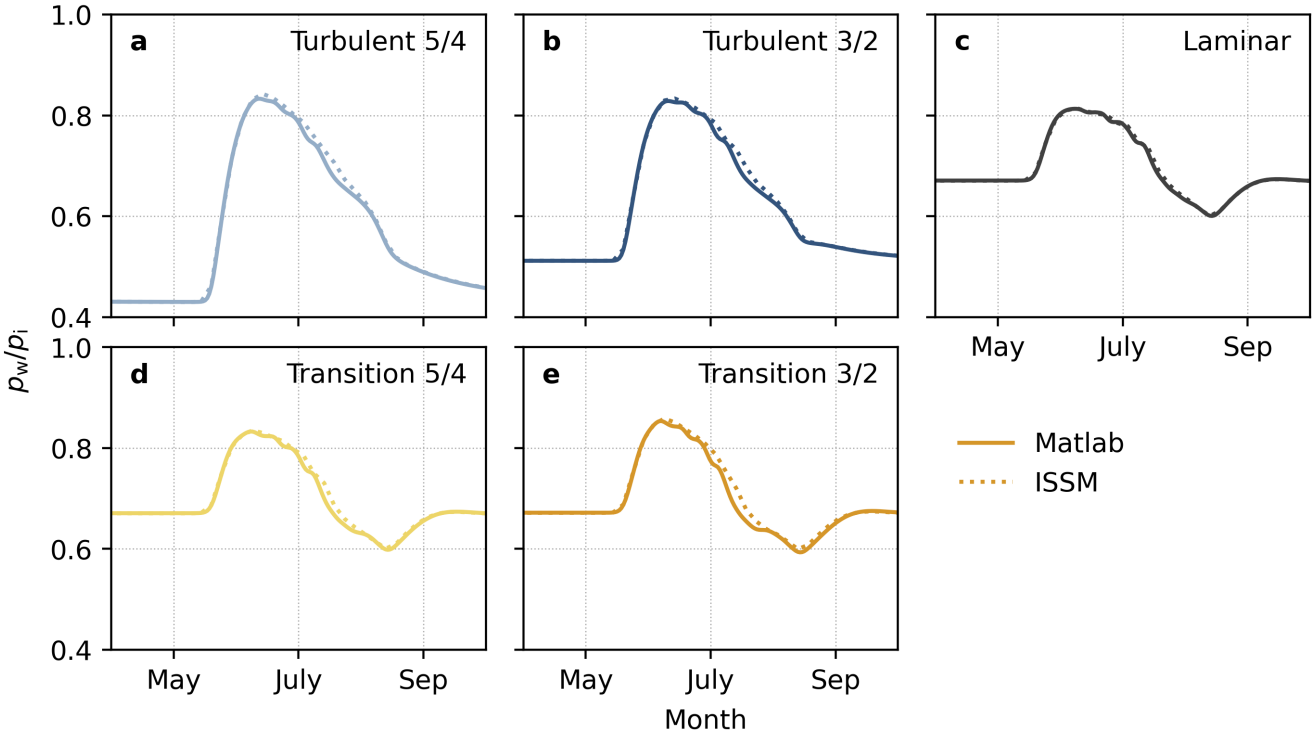

Fig. S8. Model verification against the ISSM implementation of GlaDS. Width-averaged floatation fraction 30 km from the terminus with synthetic melt forcing produced with the Matlab (solid) and ISSM (dotted) models.

(ISSM; Larour and others, 2012) (using branch trunk-jpl, revision 27936). We run GlaDS within ISSM using a setup identical to that described in Section 2. The water pressure produced by the two models closely agrees, with only minor differences in the behaviour following peak water pressure (Fig. S8). With these results, we are confident in the implementation of the transition models within these two independent models.

S3 SENSITIVITIES

S3.1 Melt rates

S3.1.1 Surface melt volume

The sensitivity to total surface melt volume is assessed by running the synthetic scenario with melt forcing identical to case D3 from the SHMIP experiment (Fig. S9), and by adjusting the KAN forcing to match the SHMIP D3 total melt volume (Fig. S10).

The KAN melt forcing is adjusted by setting the temperature lapse-rate equal to $\Gamma = -0.0075 °\mathrm{C\,m^{-1}}$ (to match SHMIP case D3) and solving for the multiplicative factor that yields identical total surface melt

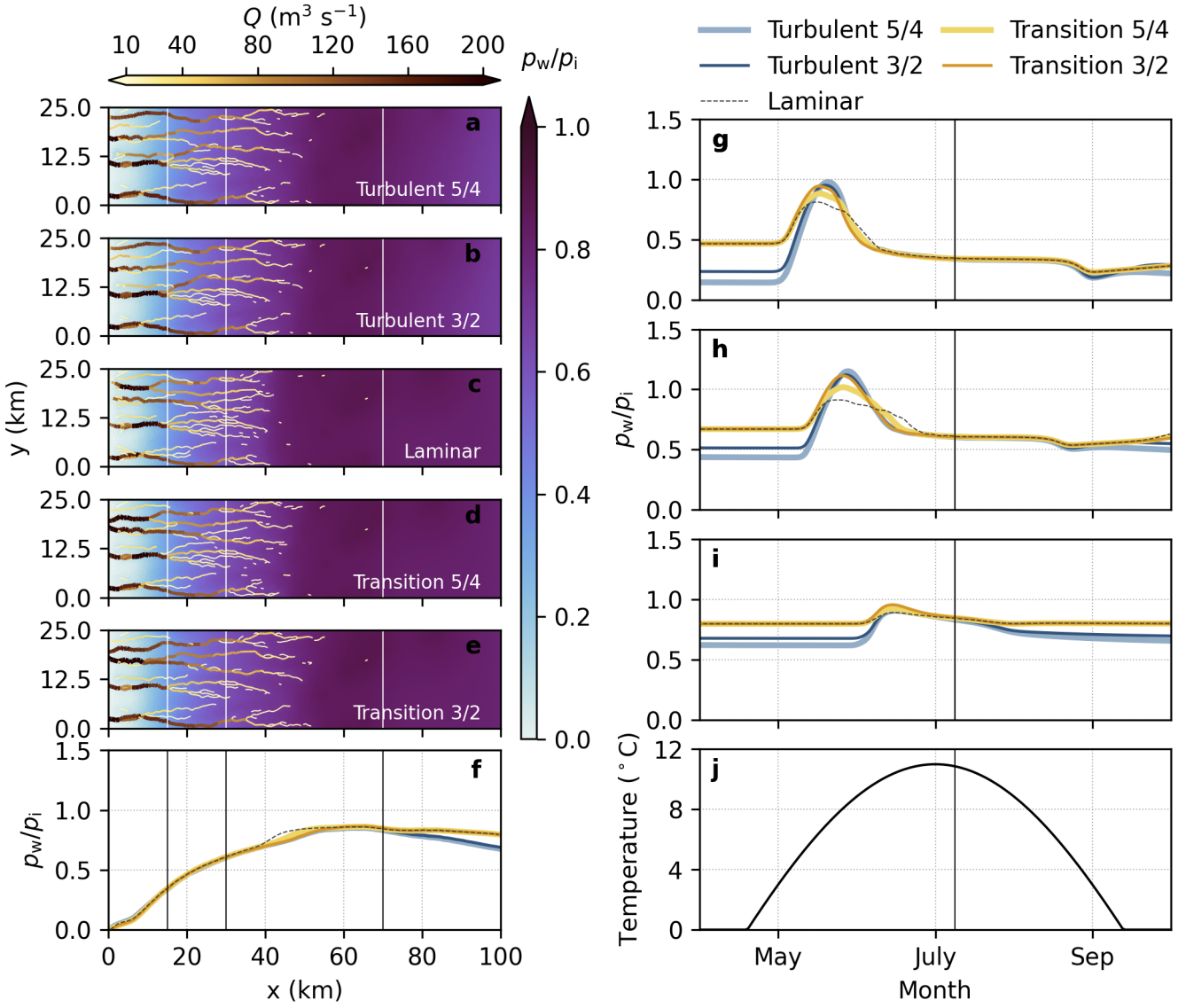

Fig. S9. Transient simulation with surface melt rates identical to SHMIP case D3. Floatation fraction $\frac{p_w}{p_i}$ and channel discharge on 9 July (a-e) for Turbulent 5/4 (a), Turbulent 3/2 (b), Laminar (c), Transition 5/4 (d) and Transition 3/2 (e) models, and width-averaged floatation fraction on 9 July (f). Width-averaged pressure in bands at $x = 15 \pm 2.5$ km (g), $x = 30 \pm 2.5$ km (h), and $x = 70 \pm 2.5$ km (i) and imposed air temperature at 390 m a.s.l. used to force the degree-day model (j).

Table S3. Parameter adjustments for the sensitivity test.

Parameter	Default value	"High" channelization scenario	"Low" channelization scenario
k_s	$0.05\,\mathrm{Pa\,s^{-1}}$	$0.02\,\mathrm{Pa\,s^{-1}}$	$0.1\,\mathrm{Pa\,s^{-1}}$
k_c	$0.5\,\mathrm{m^{3/2}\,s^{-1}}$	$1.0\,\mathrm{m^{3/2}\,s^{-1}}$	$0.2\,\mathrm{m^{3/2}\,s^{-1}}$
l_c	10 m	25 m	10 m

volumes.

S3.1.2 Basal melt rate

Sensitivity to basal melt rate is tested by decreasing the prescribed basal melt rate from $0.05\,\mathrm{m\,w.e.\,a^{-1}}$ to $0.01\,\mathrm{m\,w.e.\,a^{-1}}$ (i.e., a low basal friction regime). Figure S11 compares average floatation fraction 30 km from the terminus for low and high basal melt rates with KAN surface melt forcing.

Decreasing the basal melt rate decreases winter water pressure for all flux parameterizations, but has a limited impact once surface melt drives drainage development (Fig. S11). The decreased winter water pressure highlights that including a realistic basal melt rate is important for obtaining broadly more realistic results and for producing a stronger late-summer pressure minimum for the laminar and transition models.

S3.2 Parameter sensitivity

S3.2.1 Channelization

We assess how the relative performance of the flux parameterizations changes for end-members representing minimal and extensive channelization. Table S3 lists the parameters tuned to run these scenarios. Figures S12 and S13 present the floatation fraction, channel discharge, and Reynolds number for the high channelization scenario. Figures S14 and S15 present the same quantities for the low channelization scenario.

S3.2.2 Englacial storage

The magnitude of pressure variations with KAN forcing is sensitive to the chosen englacial storage parameter. To constrain this sensitivity, we run the KAN experiment with the englacial storage parameter reduced from $e_v = 1 \times 10^{-4}$ to $e_v = 2 \times 10^{-5}$. This reduction in storage shortens the timescale associated with pressure adjustments and increases the magnitude of pressure variations (Fig. S16).

Reducing englacial storage increases the magnitude of the spring pressure maximum (>200% of over-

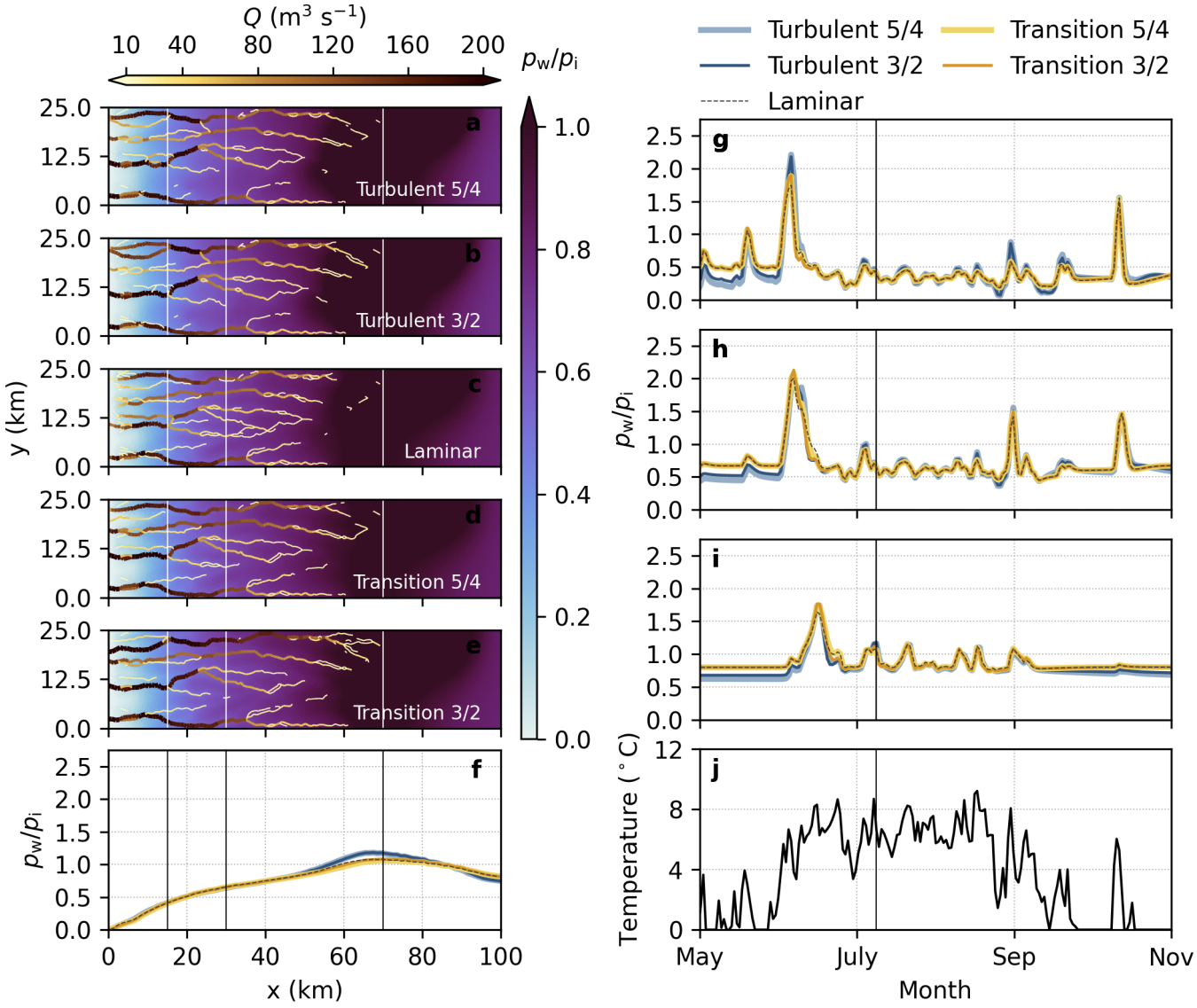

Fig. S10. Transient simulation with KAN surface melt forcing adjusted to have identical total surface melt volume as SHMIP case D3. Floatation fraction $\frac{p_w}{p_i}$ and channel discharge on 9 July (a-e) for Turbulent 5/4 (a), Turbulent 3/2 (b), Laminar (c), Transition 5/4 (d) and Transition 3/2 (e) models, and width-averaged floatation fraction on 9 July (f). Width-averaged pressure in bands at $x = 15 \pm 2.5$ km (g), $x = 30 \pm 2.5$ km (h), and $x = 70 \pm 2.5$ km (i) and imposed air temperature at 390 m a.s.l. used to force the degree-day model (j).

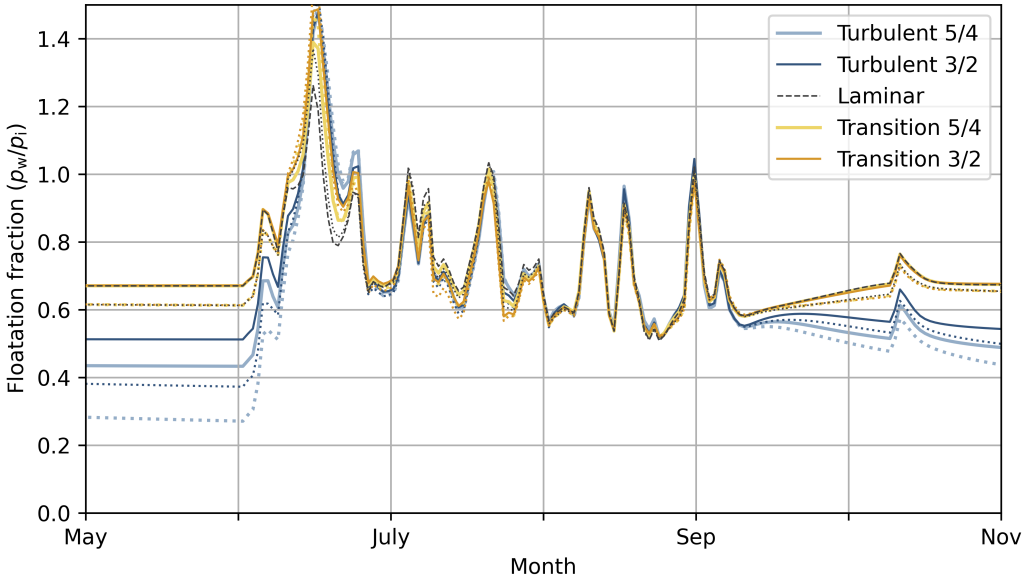

Fig. S11. Average floatation fraction within $x = 30 \pm 2.5\,\mathrm{km}$ with basal melt rates of $0.01\,\mathrm{m\,w.e.\,a^{-1}}$ (dotted) and $0.05\,\mathrm{m\,w.e.\,a^{-1}}$ (solid; dashed for the laminar model for clarity) with KAN surface melt forcing.

burden for the turbulent models), but this does not change the ordering of models in terms of winter water pressure, late-summer pressure minima, the spring pressure maximum, or internal consistency.

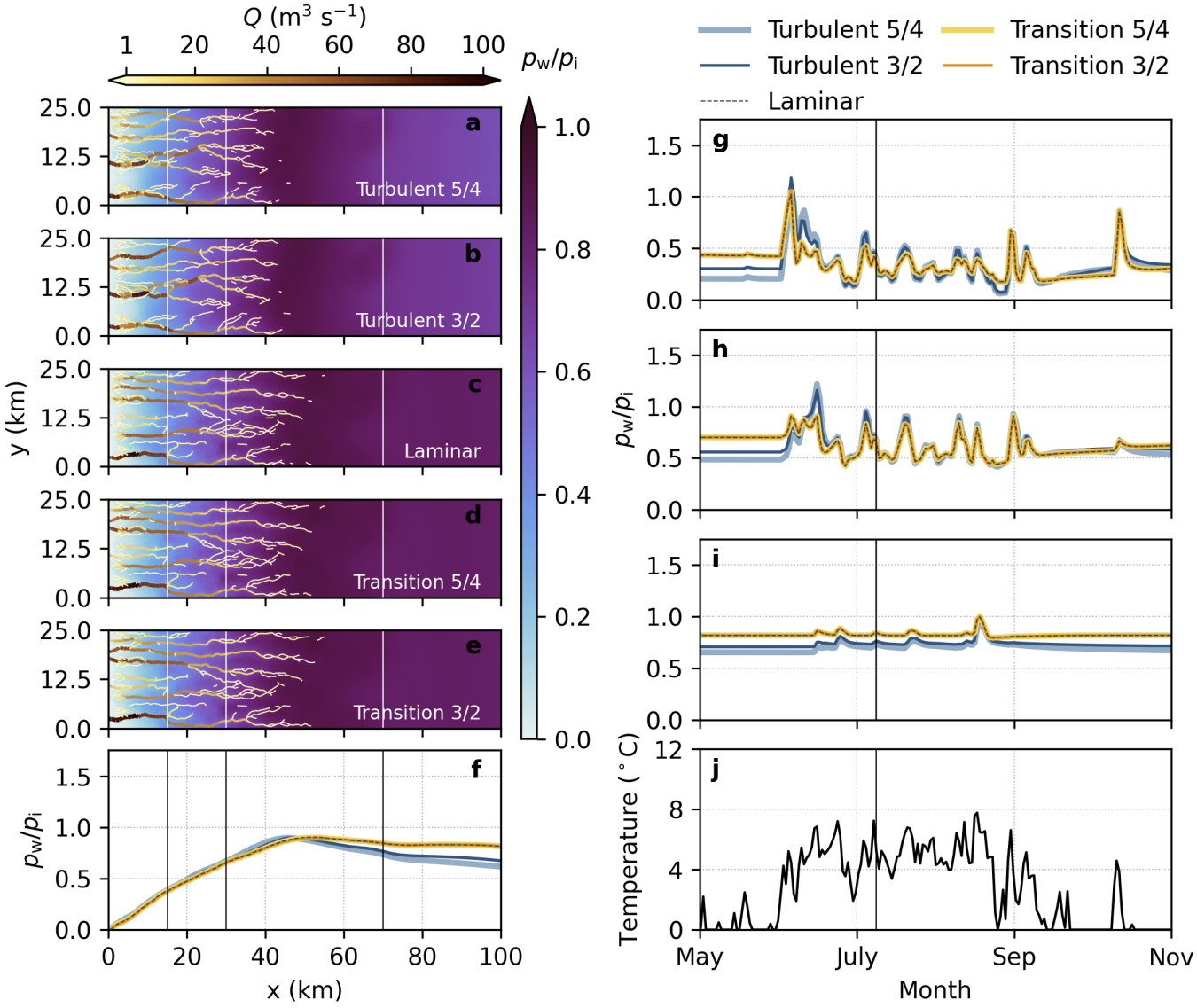

Fig. S12. Drainage configuration for "high" scenario parameters as in Table S3. Floatation fraction $\frac{p_w}{p_i}$ and channel discharge on 9 July (a-e) for Turbulent 5/4 (a), Turbulent 3/2 (b), Laminar (c), Transition 5/4 (d) and Transition 3/2 (e) models, and width-averaged floatation fraction on 9 July (f). Width-averaged pressure in bands at $x = 15 \pm 2.5$ km (g), $x = 30 \pm 2.5$ km (h), and $x = 70 \pm 2.5$ km (i) and imposed air temperature at 390 m a.s.l. used to force the degree-day model (j).

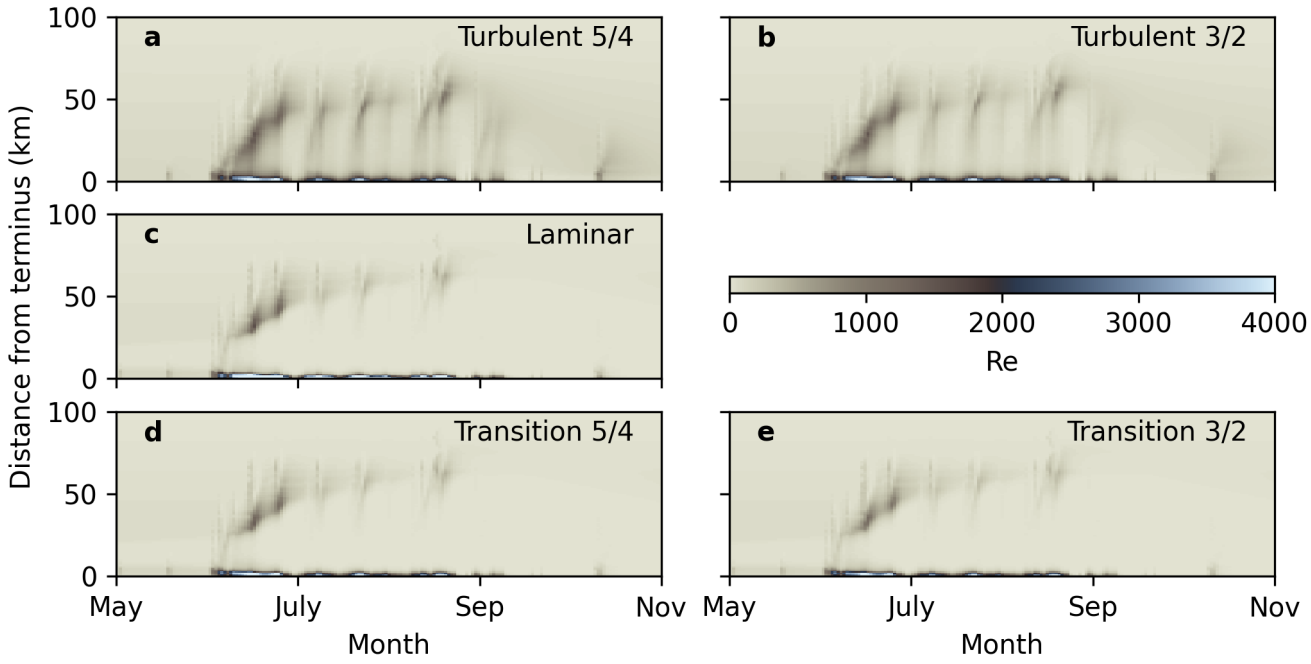

Fig. S13. Seasonal evolution of width-averaged Reynolds number and channel discharge for "high" scenario parameters as in Table S3 for Turbulent 5/4 (a), Turbulent 3/2 (b), Laminar (c), Transition 5/4 (d), and Transition 3/2 (e) models.

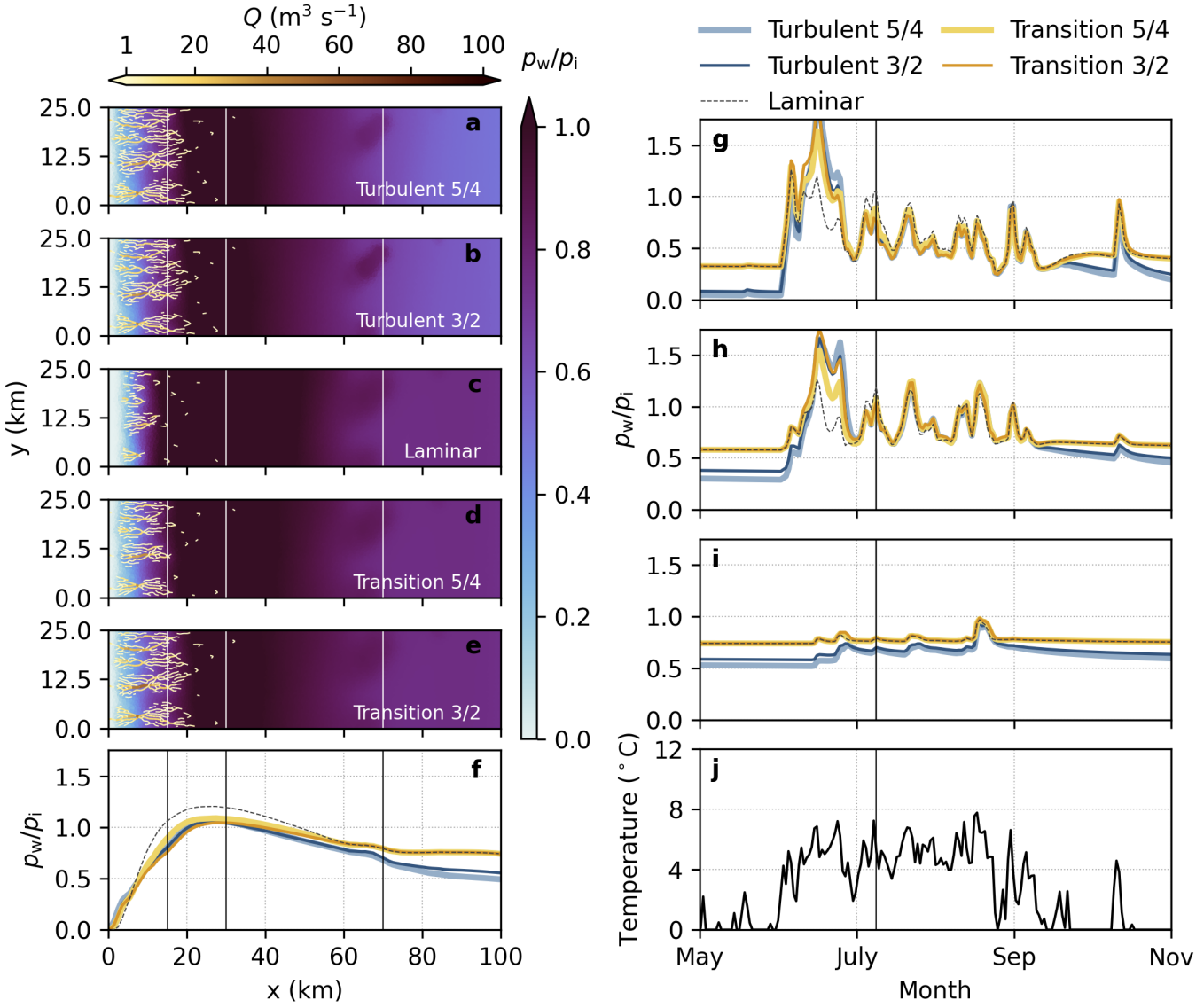

Fig. S14. Drainage configuration for "low" scenario parameters as in Table S3. Floatation fraction $\frac{p_w}{p_i}$ and channel discharge on 9 July (a-e) for Turbulent 5/4 (a), Turbulent 3/2 (b), Laminar (c), Transition 5/4 (d) and Transition 3/2 (e) models, and width-averaged floatation fraction on 9 July (f). Width-averaged pressure in bands at $x = 15 \pm 2.5$ km (g), $x = 30 \pm 2.5$ km (h), and $x = 70 \pm 2.5$ km (i) and imposed air temperature at 390 m a.s.l. used to force the degree-day model (j).

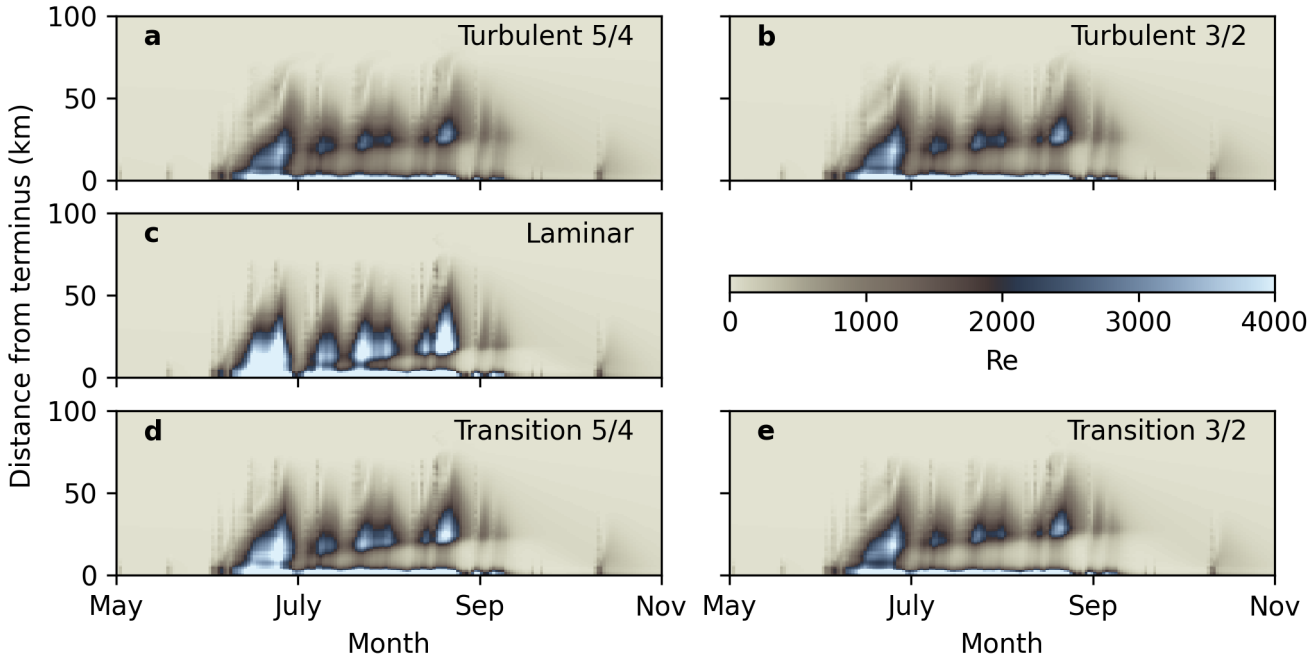

Fig. S15. Seasonal evolution of width-averaged Reynolds number for "low" scenario parameters as in Table S3 for Turbulent 5/4 (a), Turbulent 3/2 (b), Laminar (c), Transition 5/4 (d), and Transition 3/2 (e) models.

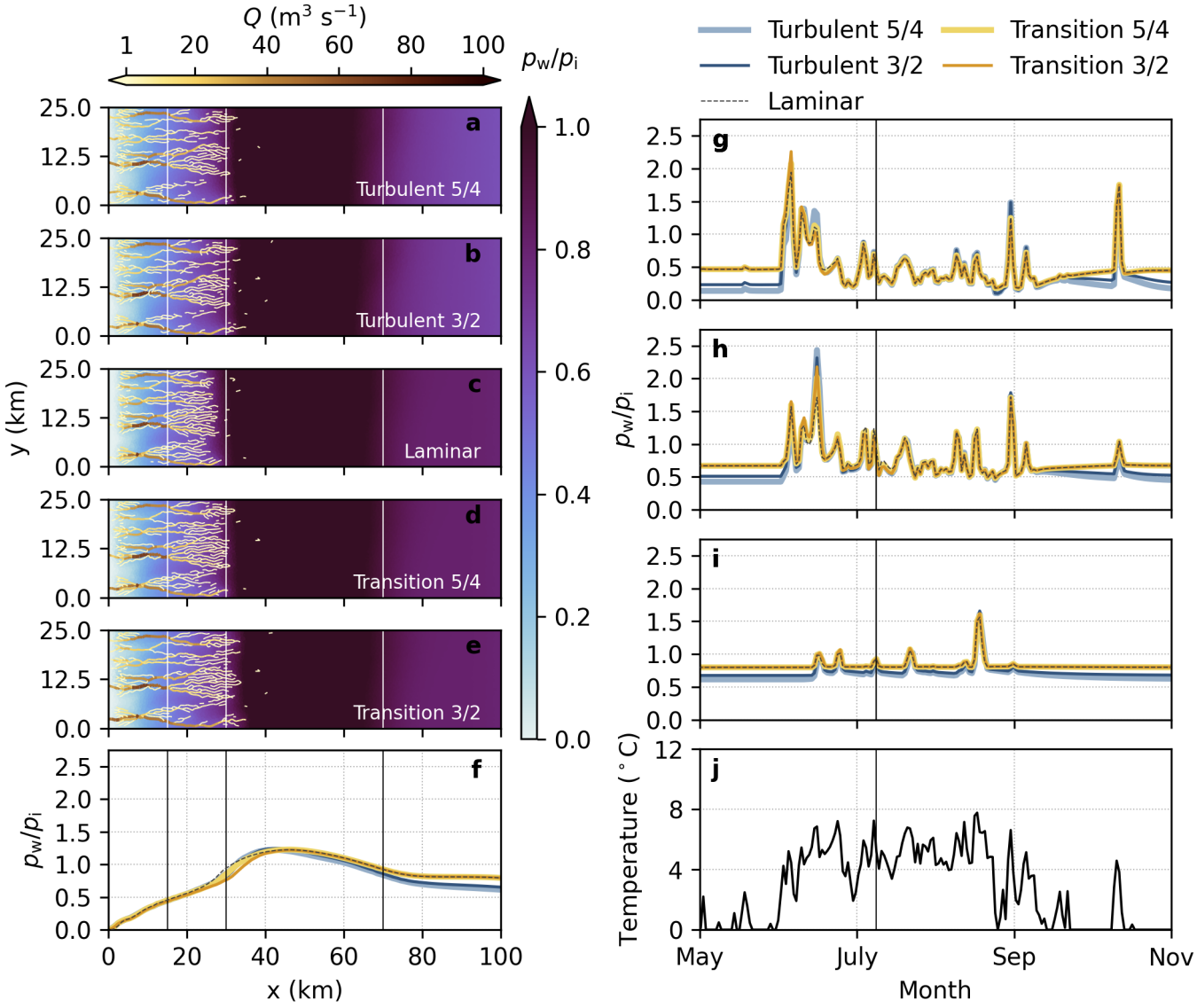

Fig. S16. KAN forcing scenario with reduced englacial storage parameter ($e_v = 2 \times 10^{-5}$ instead of the default $e_v = 1 \times 10^{-4}$). Floatation fraction $\frac{p_w}{p_i}$ and channel discharge on 9 July (a-e) for Turbulent 5/4 (a), Turbulent 3/2 (b), Laminar (c), Transition 5/4 (d) and Transition 3/2 (e) models, and width-averaged floatation fraction on 9 July (f). Width-averaged pressure in bands at $x = 15 \pm 2.5$ km (g), $x = 30 \pm 2.5$ km (h), and $x = 70 \pm 2.5$ km (i) and imposed air temperature at 390 m a.s.l. used to force the degree-day model (j).

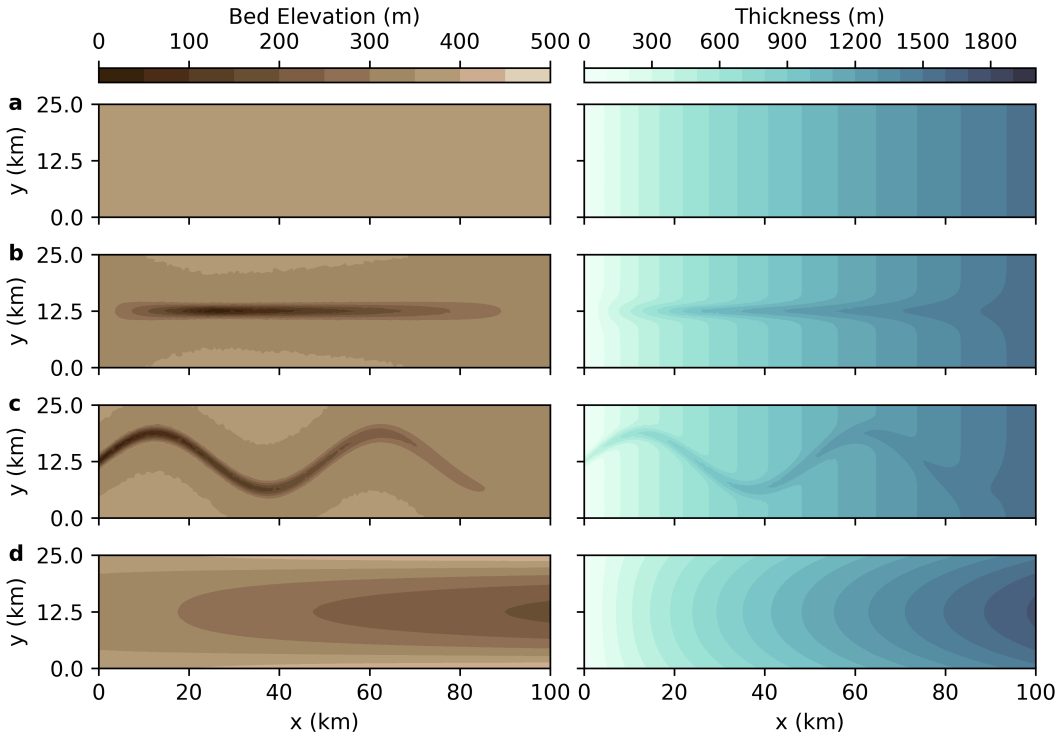

Fig. S17. Bed elevation (left) and ice thickness (right) for flat bed (a), trough (b), sinusoidal (c) and valley (d) scenarios.

S3.3 Bed topography

The simulations presented so far have used a highly idealized geometry with a flat bed. Since subglacial topography is expected to be a primary control on the position of subglacial channels in real applications (e.g., Cook and others, 2020; Dow and others, 2022; Ehrenfeucht and others, 2023), we assess the sensitivity of our results to three simple, non-flat bed representations (Fig. S17). The "trough" bed has a ∼6 km-wide, 350 m-deep trough running down the centre of the domain, intended to represent drainage through subglacial troughs in west Greenland (Porter and others, 2018). The "sinusoidal" bed extends the bed trough to reach the terminus and prescribes the trough to follow a sinusoidal path to induce lateral variation. For this case, the outlet boundary condition is modified to a no-flux condition everywhere except for a single atmospheric pressure node at the base of the trough. The "valley" bed is U-shaped and with a retrograde bed sloping downwards from 350 m at the terminus to 200 m at the upper boundary.

For the trough (Fig. S18), sinusoidal (Fig. S19) and valley (Fig. S20) beds, the width-averaged floatation fraction is not significantly affected by the bed topography aside from negative water pressure near the terminus for the sinusoidal bed as a result of the no-flux boundary condition. The sinusoidal bed produces

significantly different spatial patterns of channelization, with channels primarily following the path of the trough.

The impact of the valley bed is limited to channels near the domain margin. The marginal channels for the laminar and transition models carry slightly less discharge than in the flat bed case, but this does not noticeably affect width-average floatation fraction.

S3.4 Boundary conditions

To test the sensitivity of our results to the imposed boundary conditions, we modify the terminus boundary condition to a full floatation condition, $p_\mathrm{w} = p_\mathrm{i}$, and apply synthetic surface melt forcing. Aside from the nearest 5–10 km to the terminus, there is negligible difference in water pressure or channel discharge (Fig. S21). Compared to the atmospheric pressure case, subglacial channels fully terminate slightly further from the margin (Fig. 4).

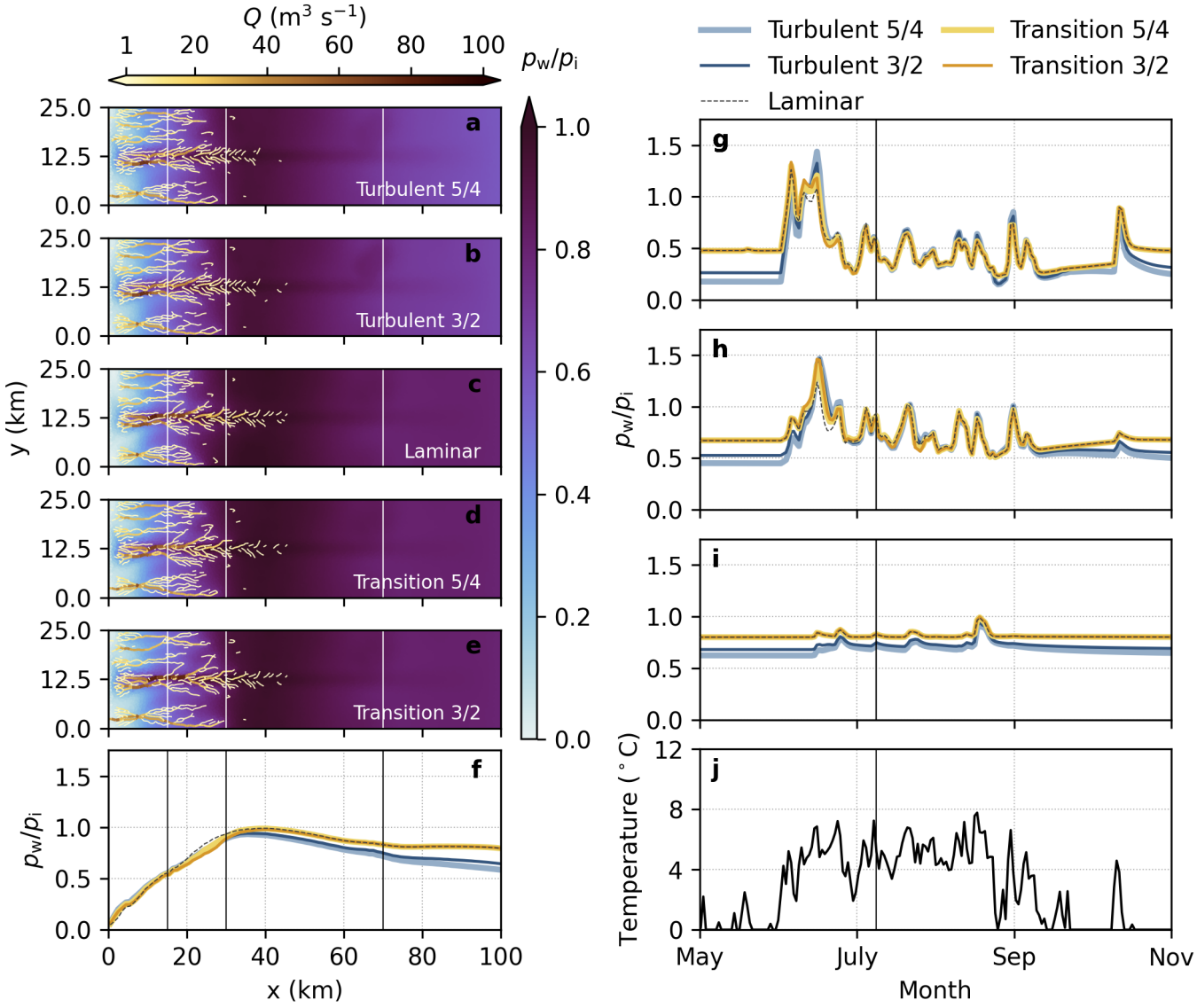

Fig. S18. Trough bed topography with KAN melt forcing. Floatation fraction $\frac{p_w}{p_i}$ and channel discharge on 9 July (a-e) for Turbulent 5/4 (a), Turbulent 3/2 (b), Laminar (c), Transition 5/4 (d) and Transition 3/2 (e) models, and width-averaged floatation fraction on 9 July (f). Width-averaged pressure in bands at $x = 15 \pm 2.5$ km (g), $x = 30 \pm 2.5$ km (h), and $x = 70 \pm 2.5$ km (i) and imposed air temperature at 390 m a.s.l. used to force the degree-day model (j).

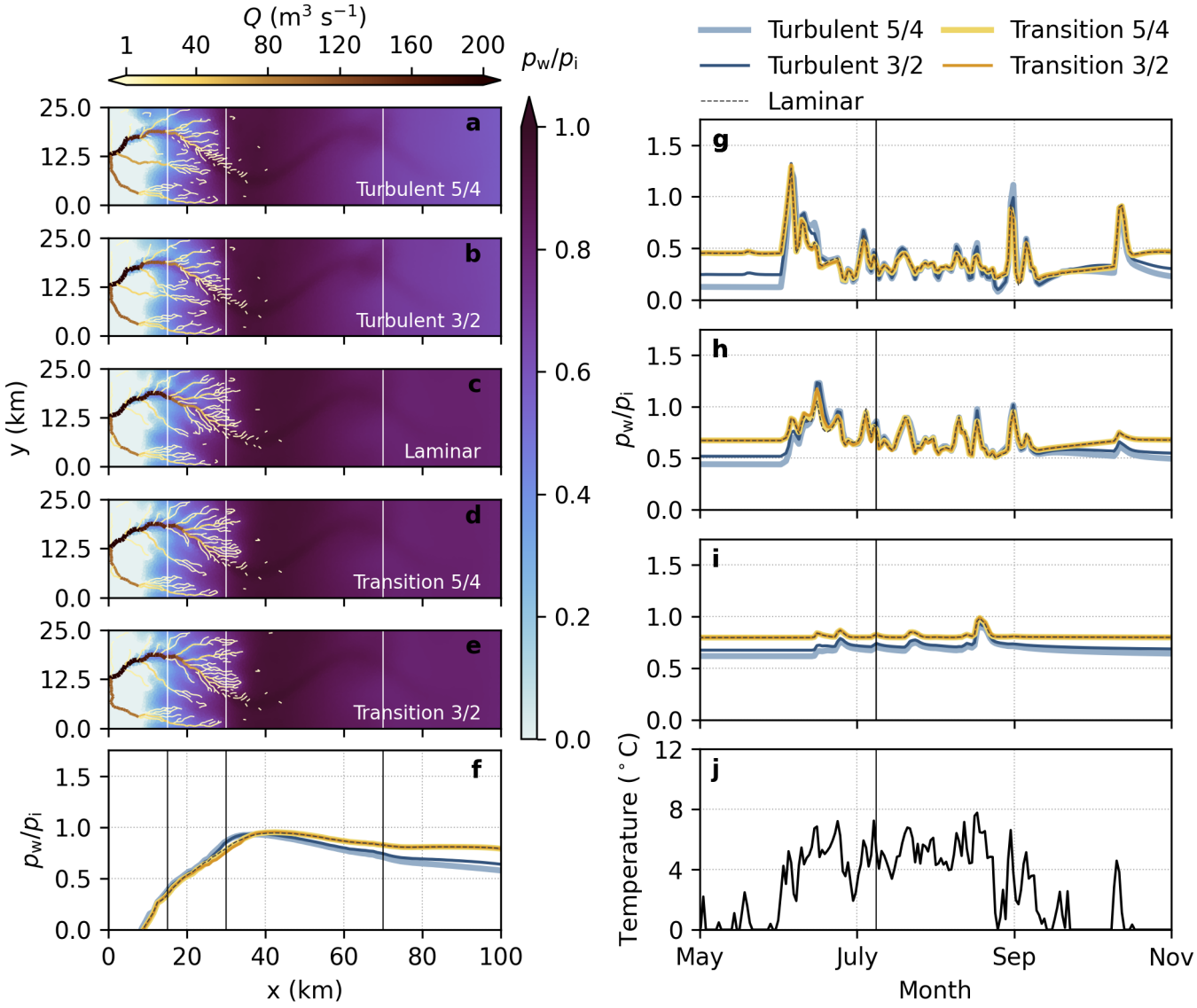

Fig. S19. Sinusoidal bed topography with KAN melt forcing. Floatation fraction $\frac{p_w}{p_i}$ and channel discharge on 9 July (a-e) for Turbulent 5/4 (a), Turbulent 3/2 (b), Laminar (c), Transition 5/4 (d) and Transition 3/2 (e) models, and width-averaged floatation fraction on 9 July (f). Width-averaged pressure in bands at $x = 15 \pm 2.5$ km (g), $x = 30 \pm 2.5$ km (h), and $x = 70 \pm 2.5$ km (i) and imposed air temperature at 390 m a.s.l. used to force the degree-day model (j).

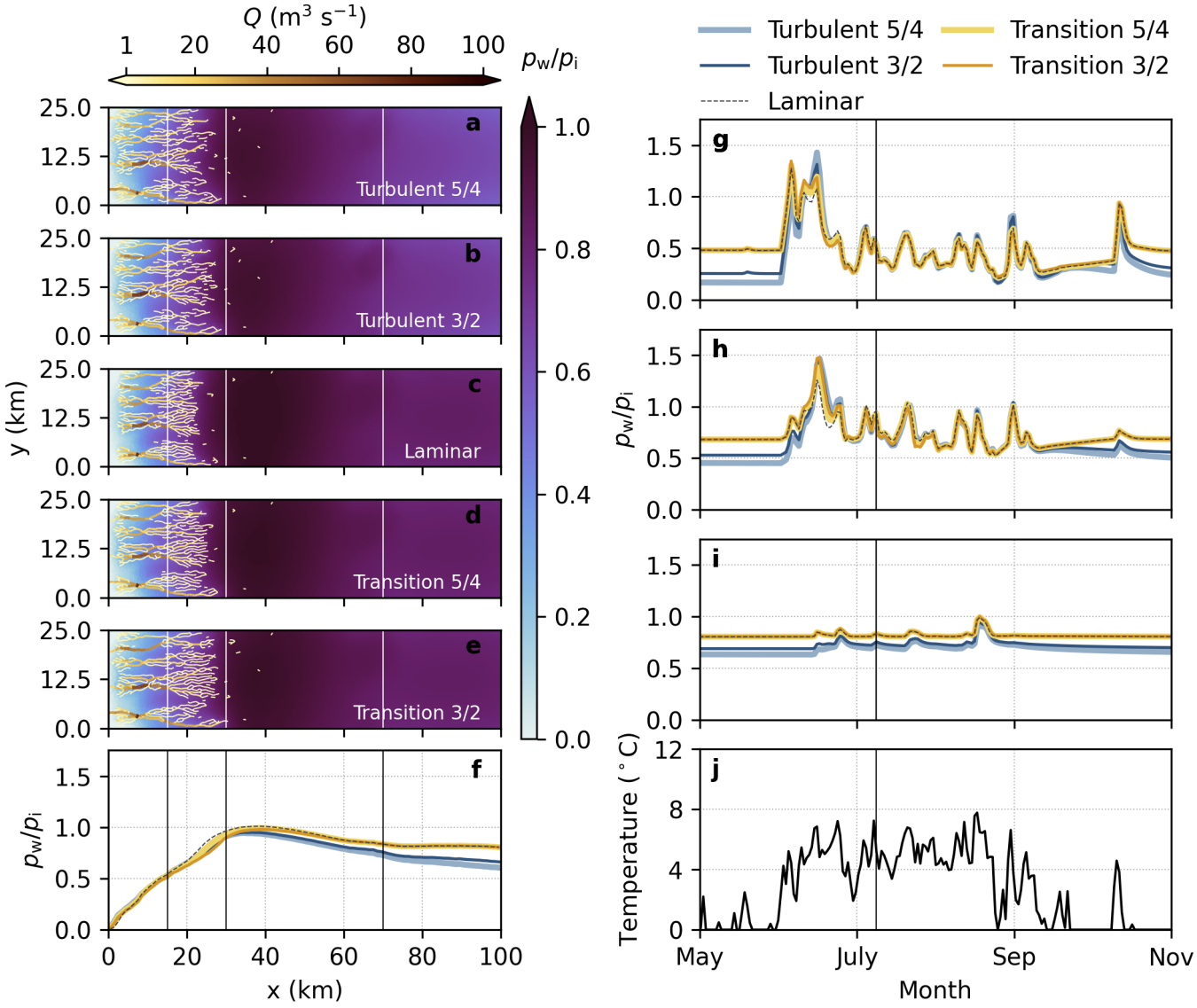

Fig. S20. Valley bed topography with KAN melt forcing. Floatation fraction $\frac{p_w}{p_i}$ and channel discharge on 9 July (a-e) for Turbulent 5/4 (a), Turbulent 3/2 (b), Laminar (c), Transition 5/4 (d) and Transition 3/2 (e) models, and width-averaged floatation fraction on 9 July (f). Width-averaged pressure in bands at $x = 15 \pm 2.5$ km (g), $x = 30 \pm 2.5$ km (h), and $x = 70 \pm 2.5$ km (i) and imposed air temperature at 390 m a.s.l. used to force the degree-day model (j).

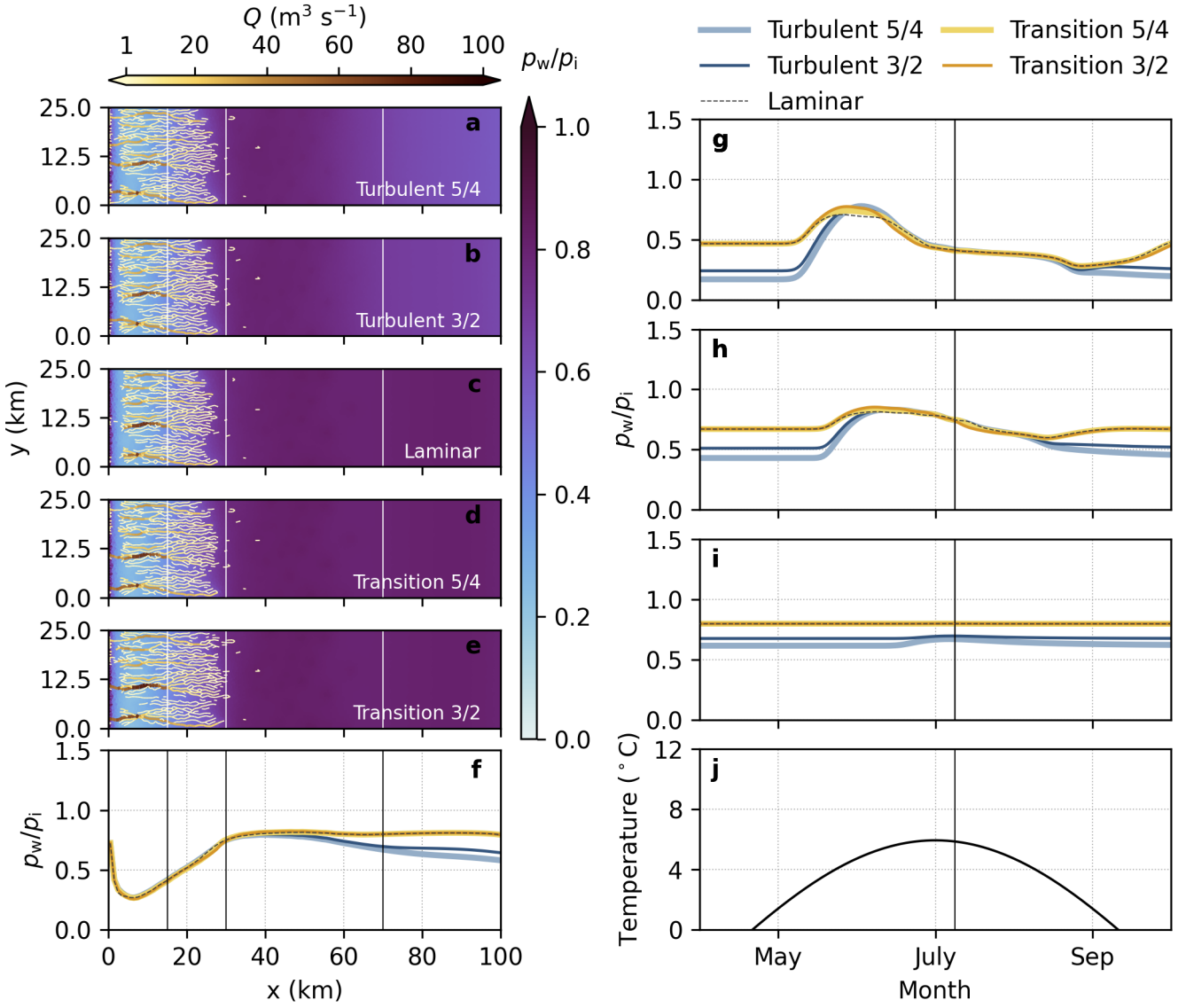

Fig. S21. Floatation boundary condition with synthetic melt forcing. Floatation fraction $\frac{p_w}{p_i}$ and channel discharge on 9 July (a-e) for Turbulent 5/4 (a), Turbulent 3/2 (b), Laminar (c), Transition 5/4 (d) and Transition 3/2 (e) models, and width-averaged floatation fraction on 9 July (f). Width-averaged pressure in bands at $x = 15 \pm 2.5$ km (g), $x = 30 \pm 2.5$ km (h), and $x = 70 \pm 2.5$ km (i) and imposed air temperature at 390 m a.s.l. used to force the degree-day model (j).

REFERENCES

Brown GO (2002) The history of the Darcy-Weisbach equation for pipe flow resistance. In *Environmental and Water Resources History Sessions at ASCE Civil Engineering Conference and Exposition 2002*, 34–43 (doi: 10.1061/40650(2003)4)

Cook SJ, Christoffersen P, Todd J, Slater D and Chauché N (2020) Coupled modelling of subglacial hydrology and calving-front melting at Store Glacier, West Greenland. *The Cryosphere*, **14**(3), 905–924 (doi: 10.5194/tc-14-905-2020)

Cook SJ, Christoffersen P and Todd J (2022) A fully-coupled 3D model of a large Greenlandic outlet glacier with evolving subglacial hydrology, frontal plume melting and calving. *Journal of Glaciology*, **68**(269), 486–502 (doi: 10.1017/jog.2021.109)

Dow CF, Kulessa B, Rutt IC, Tsai VC, Pimentel S, Doyle SH, van As D, Lindbäck K, Pettersson R, Jones GA and Hubbard A (2015) Modeling of subglacial hydrological development following rapid supraglacial lake drainage. *Journal of Geophysical Research: Earth Surface*, **120**(6), 1127–1147 (doi: 10.1002/2014JF003333)

Dow CF, Ross N, Jeofry H, Siu K and Siegert MJ (2022) Antarctic basal environment shaped by high-pressure flow through a subglacial river system. *Nature Geoscience*, 1–7 (doi: 10.1038/s41561-022-01059-1)

Downs JZ, Johnson JV, Harper JT, Meierbachtol T and Werder MA (2018) Dynamic hydraulic conductivity reconciles mismatch between modeled and observed winter subglacial water pressure. *Journal of Geophysical Research: Earth Surface*, **123**(4), 818–836 (doi: 10.1002/2017JF004522)

Ehrenfeucht S, Morlighem M, Rignot E, Dow CF and Mouginot J (2023) Seasonal acceleration of Petermann glacier, Greenland, from changes in subglacial hydrology. *Geophysical Research Letters*, **50**(1), e2022GL098009 (doi: 10.1029/2022GL098009)

Hager AO, Hoffman MJ, Price SF and Schroeder DM (2022) Persistent, extensive channelized drainage modeled beneath Thwaites Glacier, West Antarctica. *The Cryosphere*, **16**(9), 3575–3599 (doi: 10.5194/tc-16-3575-2022)

Hoffman MJ, Perego M, Price SF, Lipscomb WH, Zhang T, Jacobsen D, Tezaur I, Salinger AG, Tuminaro R and Bertagna L (2018) MPAS-Albany Land Ice (MALI): a variable-resolution ice sheet model for Earth system modeling using Voronoi grids. *Geoscientific Model Development*, **11**(9), 3747–3780 (doi: 10.5194/gmd-11-3747-2018)

How P, Abermann J, Ahlstrøm A, Andersen S, Box JE, Citterio M, Colgan W, RS F, Karlsson N, Jakobsen J, Langley K, Larsen S, Mankoff K, Pedersen A, Rutishauser A, Shield C, Solgaard A, van As D, Vandecrux B and Wright P (2022) PROMICE and GC-Net automated weather station data in Greenland (doi: 10.22008/FK2/IW73UU)

Larour E, Seroussi H, Morlighem M and Rignot E (2012) Continental scale, high order, high spatial resolution, ice sheet modeling using the Ice Sheet System Model (ISSM). *Journal of Geophysical Research: Earth Surface*, **117**(F1) (doi: https://doi.org/10.1029/2011JF002140)

Moody LF (1944) Friction factors for pipe flow. *Trans. Asme*, **66**, 671–684 (doi: 10.1115/1.4018140)

Porter C, Morin P, Howat I, Noh MJ, Bates B, Peterman K, Keesey S, Schlenk M, Gardiner J, Tomko K, Willis M, Kelleher C, Cloutier M, Husby E, Foga S, Nakamura H, Platson M, Wethington J Michael, Williamson C, Bauer G, Enos J, Arnold G, Kramer W, Becker P, Doshi A, D'Souza C, Cummens P, Laurier F and Bojesen M (2018) ArcticDEM, Version 3 (doi: 10.7910/DVN/OHHUKH), [20 October, 2022]

Sommers A, Rajaram H and Morlighem M (2018) SHAKTI: subglacial hydrology and kinetic, transient interactions v1.0. *Geoscientific Model Development*, **11**(7), 2955–2974 (doi: 10.5194/gmd-11-2955-2018)

Tsai VC and Rice JR (2010) A model for turbulent hydraulic fracture and application to crack propagation at glacier beds. *Journal of Geophysical Research: Earth Surface*, **115**(F3) (doi: 10.1029/2009JF001474)

Werder MA, Hewitt IJ, Schoof CG and Flowers GE (2013) Modeling channelized and distributed subglacial drainage in two dimensions. *Journal of Geophysical Research: Earth Surface*, **118**(4), 2140–2158 (doi: 10.1002/jgrf.20146)

Yang K and Smith LC (2016) Internally drained catchments dominate supraglacial hydrology of the southwest Greenland Ice Sheet. *Journal of Geophysical Research: Earth Surface*, **121**(10), 1891–1910 (doi: 10.1002/2016JF003927)